inorganics

MDPI

Article

Two-Dimensional Zn(II), Co(II) and Cu(II) Metal–Organic Frameworks from a Symmetric Maleamate Linker

Darragh McHugh [1,2], Andreas Kourtellaris [3], Bhawna Kumari [1,4], Joan Torrent [5], Júlia Mayans [5], Soumya Mukherjee [1,4] and Constantina Papatriantafyllopoulou [1,2,*]

1 SSPC Research Ireland Centre for Pharmaceuticals; darragh.mchugh@universityofgalway.ie (D.M.); bhawna.kumari@ul.ie (B.K.); soumya.mukherjee@ul.ie (S.M.)
2 School of Biological and Chemical Sciences, College of Science and Engineering, University of Galway, H91 TK33 Galway, Ireland
3 Department of Life Sciences, School of Sciences, European University Cyprus, 6 Diogenis Str., Engomi, P.O. Box 22006, Nicosia 1516, Cyprus; a.kourtellaris@euc.ac.cy
4 Bernal Institute, Department of Chemical Sciences, University of Limerick, V94 T9PX Limerick, Ireland
5 Departament de Química Inorgànica i Orgànica, Secció Inorgànica and Institute of Nanoscience (IN2UB) and Nanotechnology, Universitat de Barcelona, Martí i Franquès 1-11, 08028 Barcelona, Spain; joan.torrent@ub.edu (J.T.); julia.mayans@ub.edu (J.M.)
* Correspondence: c.papatriantafyllopo@universityofgalway.ie

Abstract

Self-assembly of the symmetric diamide linker N,N′-(1,4-phenylene)bis(maleamic acid) (p-H_2pbm) with Zn(II), Co(II), and Cu(II) affords a structurally related family of two-dimensional coordination frameworks, OnG7-M (M = Zn, Co, Cu). Single-crystal X-ray diffraction of OnG7-Zn reveals a layered sql network constructed from four-connected dinuclear $[Zn_2(COO)_4(DMF)_2]$ paddlewheel nodes joined by ditopic p-pbm^{2-} linkers. The linker provides carboxylate coordination sites, while short interlayer amide-N···O contacts are consistent with hydrogen bonding; the amide H atoms were not located crystallographically. Thermogravimetric analysis reveals multistep mass loss including solvent removal and framework decomposition. Experiments with solvent-exchanged and dried OnG7-Zn showed depletion of 6-mercaptopurine from ethanol over 7 days and rapid release from the recovered material in phosphate-buffered saline at 37 °C. Magnetic susceptibility measurements on OnG7-Cu reveal strong antiferromagnetic coupling, with J = −158 cm^{-1}, consistent with a carboxylate-bridged Cu(II) dimer. These results connect linker-directed framework assembly with distinct uptake/release and magnetic measurements on the Zn and Cu analogues, respectively.

Keywords: metal–organic frameworks; amide-functionalised linker; 2D coordination polymer; drug loading and release; 6-Mercaptopurine; antiferromagnetic coupling

Check for updates

Academic Editor: Koichiro Takao

Received: 4 September 2026
Revised: 5 November 2026
Accepted: 9 November 2026
Published: 14 November 2026

Copyright: © 2026 by the authors. Licensee MDPI, Basel, Switzerland. This article is an open access article distributed under the terms and conditions of the Creative Commons Attribution (CC BY) license.

1. Introduction

Metal–organic frameworks (MOFs) have attracted considerable research interest over the past two decades owing to their exceptionally high porosity, large surface area, and structural tunability, which make them suitable for a wide range of applications [1–5]. Beyond three-dimensional architectures, two-dimensional (2D) MOFs have attracted increasing attention because their extended layers can provide high surface accessibility and short diffusion pathways, while interlayer interactions such as hydrogen bonding, π–π stacking, or van der Waals contacts can introduce additional structural and chemical features [6–9].

The combination of porosity, tuneable host–guest interactions, and compositional flexibility has positioned MOFs as candidates for drug delivery and biomedical applications [10–20]. Selected MOFs can combine high drug loading with tuneable stability and, in suitable cases, biocompatibility and scalable synthesis, offering potential routes to address limitations of conventional formulations, including poor stability or solubility of the active pharmaceutical ingredient, uncontrolled release, and systemic toxicity. Numerous MOFs such as ZIF-8, UiO-66, MIL-100(Fe), MIL-101(Cr), and PCN-224 have demonstrated high encapsulation efficiency and, in some cases, selective delivery to target sites [21–25]. The layered architecture of 2D MOFs can facilitate rapid loading and release while offering opportunities to engineer binding sites through linker design. Recent reports of MOF nanosheets have demonstrated high drug payloads and stimulus-responsive release, including pH- or redox-triggered delivery in physiological media, making 2D MOFs attractive candidates for the development of efficient and responsive drug-delivery systems [26–28]. Across these systems, the chemical nature of the accessible framework surface and the stability of the material in relevant media are critical. Drug uptake may involve adsorption at accessible internal and external surfaces, whereas release reflects the combined effects of host–guest interactions, accessibility and diffusion pathways, and framework persistence or degradation under the release conditions [29,30].

Linker functionalisation provides a direct route to tailoring drug–framework interactions. Among functional groups, amide motifs introduce hydrogen-bond donors and acceptors and can modulate linker flexibility and hydrophilicity [31,32]. Amide-functionalised dicarboxylate linkers and their metal–organic frameworks are well established; for example, amide-containing dicarboxylates have been used to construct Zn paddlewheel frameworks [31].

With the above in mind, we investigated N,N′-(1,4-phenylene)bis(maleamic acid), denoted as p-H_2pbm (Scheme 1), as a symmetric ditopic linker bearing two maleamic acid arms. The molecule and its Cu(II) complexes have been reported previously [33], yet this ligand has been unexplored in the field of MOFs. In its dianionic form, p-pbm^{2-} provides two carboxylate coordination groups and amide sites capable of additional intermolecular interactions. A related single-amide dicarboxylate linker has also been used to assemble Cu(II) sheets [34]. Our focus is the coordination and packing of the bis(maleamate) linker in the OnG7 frameworks.



Scheme 1. Reaction of p-phenylenediamine with maleic anhydride to form p-H_2pbm (DCM, 2 h, room temperature).

Herein, we report the synthesis and characterisation of the OnG7-M family (M = Zn, Co, Cu), obtained from p-H_2pbm and divalent transition-metal acetates. Single-crystal X-ray diffraction establishes a two-dimensional sql network for OnG7-Zn, while PXRD supports the structural similarity of the Co(II) and Cu(II) analogues. This extends the chemistry of the linker to a related framework series and allows distinct metal-dependent properties to be examined: 6MP uptake/release for OnG7-Zn and magnetic exchange for OnG7-Cu. MOF-based 6MP delivery has precedents in ZIF-8 and a glutathione-responsive system [35,36]. Here, the specific contribution is the bis(maleamate)-based framework architecture and its characterisation across three metals; the uptake/release study and the expected antiferromagnetic response of the Cu analogue provide complementary descriptions of this family.

2. Results and Discussion

2.1. Synthesis

Our group has focused on the synthesis and characterisation of MOFs with drug-delivery or sensing properties based primarily on imine-containing ligands [10,11,37–39]. In the present work, this strategy is extended to a symmetric amide-containing dicarboxylate linker. The amide groups introduce hydrogen-bond donors and acceptors alongside the carboxylate coordination sites.

The organic linker p-H_2pbm was synthesised by the nucleophilic ring opening of maleic anhydride with *p*-phenylenediamine in dichloromethane at room temperature. After 2 h, the bis(maleamic acid) derivative was isolated as a yellow solid and used for subsequent coordination reactions (Scheme 1). The identity of *p*-H_2pbm was confirmed by ^{1}H and ^{13}C NMR spectroscopy (Figure S2). The ^{1}H NMR spectrum exhibits resonances attributable to the carboxylic acid and amide protons at δ 13.11 and 10.44 ppm, respectively, along with an aromatic singlet at δ 7.59 ppm and two doublets for the olefinic protons at δ 6.46 and 6.31 ppm (J = 12.1 Hz). The ^{13}C NMR spectrum displays six resonances, including distinct carboxylic acid and amide carbonyl signals at δ 166.8 and 163.0 ppm, respectively, consistent with the expected symmetry of the bis(maleamic acid) linker.

Systematic variation in reaction temperature, solvent volume, reaction time, and metal loading enabled access to three related coordination frameworks, OnG7-M (M = Zn, Co, and Cu). OnG7-Zn formed crystals rapidly, within ca. 30 min. The Co(II) analogue crystallised more slowly, giving green plate-like crystals after ca. 3 h, suggesting metal-dependent differences in crystallisation behaviour. The OnG7-Cu preparation employed a larger metal excess, affording a crystalline green powder after 24 h. The different crystallisation times and morphologies are consistent with the known sensitivity of coordination-polymer assembly to metal-ion identity, coordination kinetics, and reaction concentration.

FTIR spectroscopy provided initial evidence for incorporation of the amide/carboxylate linker across the series (Figure S3). The spectra of OnG7-Zn, OnG7-Co, and OnG7-Cu retain ligand-based vibrational features, including bands in the 1660–1650 cm^{-1} region associated with amide/carboxylate carbonyl-containing modes, bands in the 1555–1550 and 1385–1380 cm^{-1} regions consistent with contributions from carboxylate, amide and aromatic vibrations, and a low-frequency aromatic out-of-plane bending feature.

2.2. Description of Structures

The OnG7-M frameworks are based on the dianionic linker p-pbm^{2-} and differ in terms of the identity of the coordinated metal ion, giving OnG7-Zn, OnG7-Co, and OnG7-Cu. Single-crystal X-ray diffraction data were obtained for OnG7-Zn, which is, therefore, discussed in detail as the structural representative of the series.

OnG7-Zn crystallises in the triclinic space group P1 and forms a two-dimensional coordination network containing dinuclear paddlewheel nodes (Figure 1). Each local node comprises a $[Zn_2(COO)_4(DMF)_2]$ coordination motif: four syn–syn bridging carboxylate groups surround the Zn_2 pair, and one terminal DMF molecule occupies the axial site of each Zn(II) centre. Each Zn is, thus, five-coordinate, with four carboxylate O donors from four distinct p-pbm^{2-} linkers and one DMF O donor. Each carboxylate end of p-pbm^{2-} bridges two Zn centres within one node; the second end bridges the Zn pair of a neighbouring node. The complete linker is, therefore, μ_4 with respect to individual Zn centres but ditopic with respect to the dinuclear nodes. The local node description is distinct from the framework repeat composition, $[Zn_2(\text{p-pbm})_2(DMF)_2]$, with additional lattice DMF and H_2O in the formulated material.

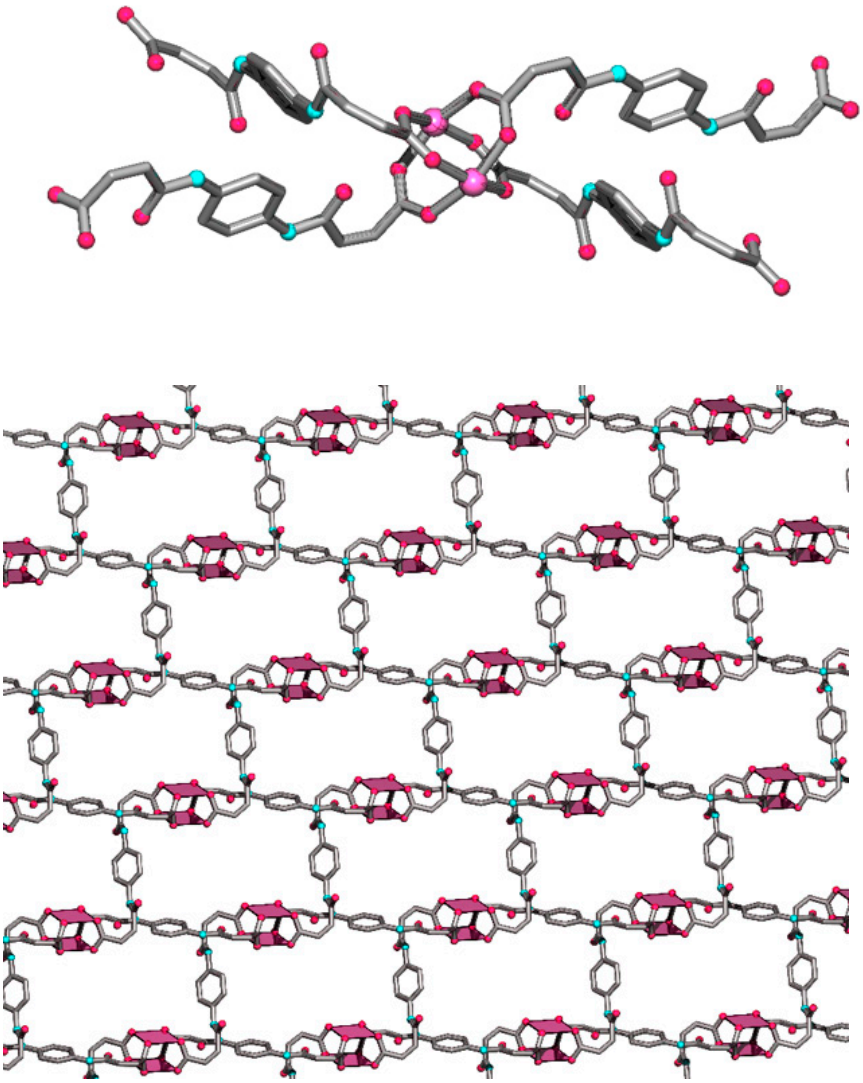


Figure 1. Top: representation of the paddlewheel SBU and ligand connectivity in OnG7-Zn. Bottom: the 2D network in OnG7-Zn. Colour code: N (blue), Zn (magenta), O (red), and C (grey). Hydrogen atoms and lattice solvent molecules are omitted for clarity.

Each Zn(II) centre adopts a distorted square-pyramidal geometry. Reducing each Zn_2 paddlewheel to a node and each bridging p-pbm^{2-} linker to an edge gives a four-connected two-dimensional sql net with point symbol $\{4^4 \cdot 6^2\}$. Each node is linked to four neighbouring nodes; μ_4 describes the linker's metal coordination rather than its topological connectivity. Short amide-N···O contacts occur both between and within the coordination layers (Table 1 and Figure 2). In the deposited model, N1···O13 = 2.770 Å and N2···O14 = 2.825 Å connect adjacent layers, whereas N3···O11 = 2.937 Å and N4···O12 = 2.865 Å lie within a layer. The amide H atoms were not crystallographically located. These donor–acceptor contacts are, therefore, consistent with the proposed N–H···O hydrogen bonding. Their contribution to layer cohesion is an interpretation of the packing geometry.

Table 1. Short amide-N···O contacts calculated from the deposited OnG7-Zn model.

Contact	Acceptor Position	N···O/Å	Relation
N1···O13	x − 1, y, z	2.770	Interlayer
N2···O14	x, y + 1, z	2.825	Interlayer
N3···O11	x, y, z	2.937	Intralayer
N4···O12	x + 1, y − 1, z	2.865	Intralayer

O11–O14 are amide carbonyl O atoms. Amide H positions were not determined.

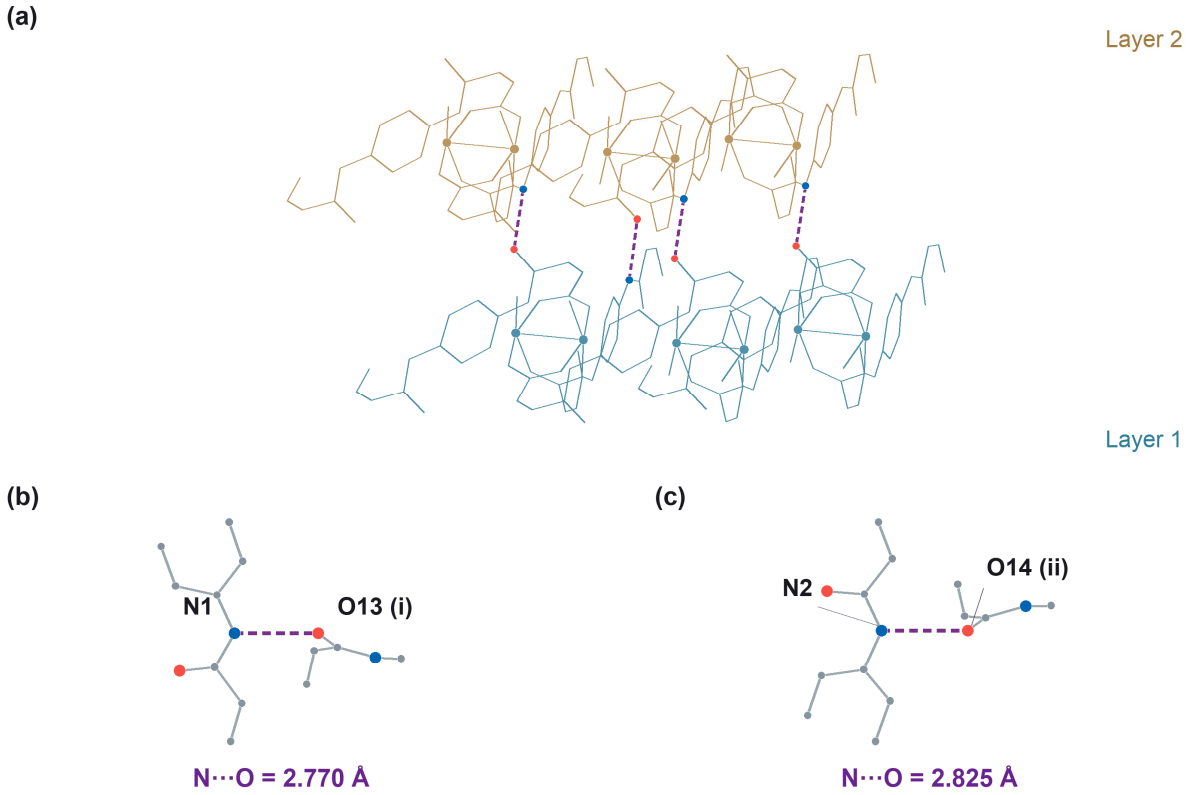


Figure 2. Selected interlayer N···O contacts in OnG7-Zn. (**a**) Portions of two adjacent coordination layers, coloured blue and gold; larger circles denote Zn centres. (**b**,**c**) Enlarged N1···O13(i) and N2···O14(ii) contacts, respectively. Purple dashed lines indicate short donor–acceptor contacts consistent with proposed N–H···O hydrogen bonding. C, grey; N, blue; and O, red. Symmetry operations: (i) x − 1, y, z and (ii) x, y + 1, z. H atoms and lattice guests are omitted throughout; coordinated DMF is also omitted in (**a**).

2.3. Thermogravimetric Analysis

The thermal behaviour of the parent OnG7 series was examined by thermogravimetric analysis under N_2 (Figure 3a). All three materials exhibit multistep mass-loss profiles. The losses up to 150 °C are 9.0% for OnG7-Zn, 3.4% for OnG7-Co and 4.3% for OnG7-Cu, which is compatible with the removal of weakly held volatile guests, although the evolved species were not identified. The cumulative losses to 290 °C are 26.2, 25.0 and 37.7%, respectively, compared with nominal total solvent fractions of 24.4, 24.7 and 24.5% for loss of three DMF molecules and one water molecule from $[M_2(p\text{-}pbm)_2(DMF)_2]\cdot DMF\cdot H_2O$. The full comparison of calculated solvent fractions and observed interval losses is provided in Table S2. The Zn and Co losses are close to the nominal solvent fractions, without identifying the species lost. The Cu loss exceeds its nominal solvent fraction by 13.2 percentage points. Its derived DTG curve (Figure 3b) shows a relatively sharp mass-loss-rate peak near 220 °C, whereas

the Zn and Co curves show broader features in this region. The distinct thermal behaviour of OnG7-Cu may reflect differences in guest content or overlap with ligand decomposition. Further mass loss at higher temperatures is consistent with progressive decomposition.

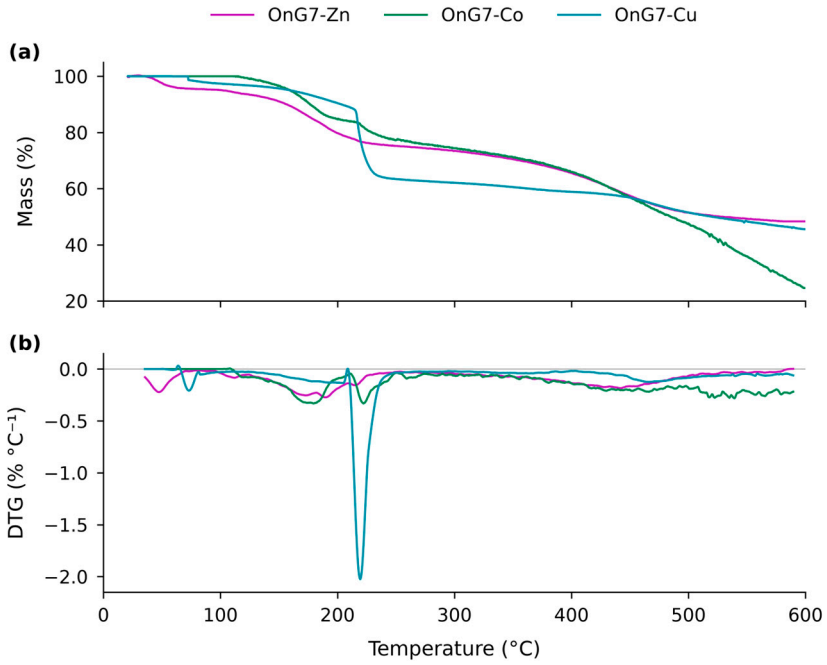


Figure 3. (**a**) TG traces and (**b**) DTG curves derived from the corresponding traces for the parent OnG7-Zn, OnG7-Co and OnG7-Cu samples. DTG is expressed as d(mass %)/dT.

2.4. Drug Loading and Release Studies

Following preliminary screening experiments with several therapeutics (doxorubicin, carbamazepine and 5-fluorouracil), 6-mercaptopurine (6MP) was selected as a model drug. OnG7-Zn was selected for the uptake and release experiments to examine drug uptake after solvent exchange and drying, and release in a phosphate-containing medium. The 6MP is a thiopurine antimetabolite used in combination maintenance regimens for acute lymphoblastic leukaemia [40,41]. Given dose-limiting systemic toxicities, drug-carrier systems remain of interest as routes to modulate exposure and reduce off-target effects.

The activated sample retains resolved diffraction peaks, showing that a crystalline component remains after treatment (Figure S8). Changes in peak positions, relative intensities and profile shape accompany activation. A Le Bail fit with the parent cell reproduces the main reflections but leaves four reflections unindexed, at 6.82°, 9.84°, 10.86° and 14.86° 2θ (Figure S10). Activation, therefore, retains a parent-related crystalline component but is accompanied by a partial structural change.

Solvent-exchanged and dried OnG7-Zn was stirred at room temperature with 6-mercaptopurine monohydrate (6MP·H_2O, 30 mg) in ethanol (10 mL). At defined time points, aliquots were centrifuged and the supernatant was analysed by UV–vis spectroscopy. The absorbance at 310 nm decreased by 53.4% between day 0 and day 7 (Figure S4), indicating uptake of 6MP from solution. Because complete dissolution of 6MP at this nominal concentration was not confirmed, and uptake had not reached a plateau within 7 days, the result is reported as solution depletion rather than as a loading capacity. Solution depletion also cannot distinguish uptake within interlayer regions from adsorption at external surfaces.

The FT-IR spectrum of 6MP@OnG7-Zn was compared with those of the parent material and free 6MP (Figure S7). The loaded sample retains prominent parent-material bands near 1563, 1512, 1306, 1243, 1190 and 841 cm^{-1}. Overlapping fingerprint features

prevent an unambiguous assignment of additional contributions from 6MP. The comparison supports retention of major parent-material vibrational features. The crystalline state after drug loading remains undetermined, and the spectra do not assign a drug location or binding mode.

Drug release from 6MP@OnG7-Zn was evaluated in phosphate-buffered saline (PBS, pH 7.4) at 37 °C using UV–vis spectroscopy (Figure S5). A rapid increase in the characteristic 6MP absorbance was observed during the initial stages of release, followed by minimal further change at longer times, with the release signal approaching a plateau within approximately 1 h. No recoverable solid remained after release, so post-release structural analysis could not be performed. This observation does not quantify Zn leaching or establish a phosphate-specific dissociation pathway. Because loading and release were measured in different media, solvent effects, desorption and framework disassembly cannot be excluded from these measurements.

2.5. Magnetism Studies

Magnetic susceptibility measurements (Figure 4) were performed on pressed polycrystalline samples of OnG7-Cu under a dc field of 0.3 T over 2–300 K and are presented as $\chi_M T$ *vs* T. At 300 K, $\chi_M T = 0.409$ cm^3 mol^{-1} K, which is significantly lower than expected for two uncoupled Cu(II) ions ($S = 1/2$, $g \approx 2$), and is consistent with strong antiferromagnetic coupling within the dinuclear unit. This behaviour is anticipated for two Cu(II) centres bridged by *syn–syn* carboxylate ligands. Upon cooling, $\chi_M T$ decreases continuously and the data can be modelled using PHI to give $J_{12} = -158(2)$ cm^{-1}, g = 2.02(1), and a minor paramagnetic contribution (~5%), which is apparent as a subtle upturn in χ_M below ~40 K [42].

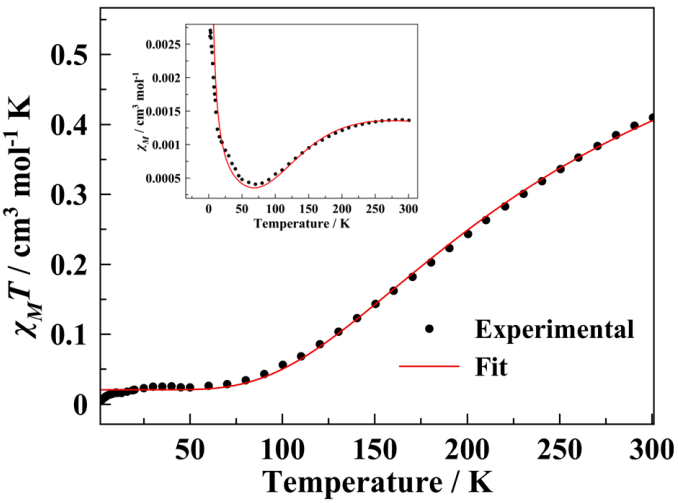


Figure 4. χ_MT vs. T for OnG7-Cu (2–300 K) measured under a 0.3 T dc field; inset: χ_M vs. T. The solid line represents the best fit.

3. Materials and Methods

3.1. General and Physical Measurements

Syntheses were performed under aerobic conditions, using materials as received. Elemental analyses (C, H, and N) were performed in-house at the University of Galway, School of Biological and Chemical Sciences. IR spectra (4000–400 cm^{-1}) were recorded using a PerkinElmer 16PC FT-IR spectrometer. Magnetic susceptibility measurements were performed on pressed polycrystalline samples of OnG7-Cu over 2–300 K under a dc field of 0.3 T using a Quantum Design MPMS-XL SQUID magnetometer at the CCiT Magneto-

chemistry Unit (University of Barcelona). Diamagnetic corrections were estimated using Pascal's constants [43]. TGA experiments were performed using a Rheometric Scientific STA625 thermal analyser (Piscataway, NJ, USA). Samples were heated from 20 to 600 °C at 20 °C min^{-1} in open aluminium crucibles under a nitrogen purge. The instrument was calibrated using an indium standard. UV–vis measurements were performed using an Agilent Cary 5000 UV–vis–NIR spectrophotometer. Mass-loss percentages were calculated from the TG data by linear interpolation at 150 and 290 °C, retaining the original initial-mass normalisation. For DTG, the monotonic heating data above 25 °C were linearly interpolated onto a 0.5 °C grid and differentiated using a third-order Savitzky–Golay filter with a 41-point window (20 °C span). The derivative is reported as d(mass %)/dT in % $°C^{-1}$. Only values with a complete centred window are plotted (35.5–589.5 °C). The TG traces and mass-loss calculations were not smoothed.

The OnG7-Zn PXRD data compared with the single-crystal model were collected at room temperature using a PANalytical Aeris diffractometer operated at 40 kV and 7.5 mA with Cu Kα radiation ($K\alpha_1$ = 1.540598 Å; $K\alpha_2$ = 1.544426 Å). For the as-synthesised sample shown in Figure S6, the crystals were filtered, washed with DMF (3 × 2 mL), dried under vacuum and measured without grinding. The calculated pattern was generated from the OnG7-Zn CIF. Calculation and display parameters are given with Figure S6. The separate comparison of as-synthesised and activated OnG7-Zn is provided in Figure S8, with the display normalisation specified in its caption. The additional FT-IR comparison of the parent material, 6MP@OnG7-Zn and free 6MP uses the available 4000–550 cm^{-1} spectral range (Figure S7).

Le Bail whole-pattern fits of the as-synthesised and activated OnG7-Zn patterns were performed over 5.1–40° 2θ using raw counts without smoothing, starting from the single-crystal cell (triclinic, P1). Cu $K\alpha_1/K\alpha_2$ (1.540598/1.544426 Å, 2:1) and pseudo-Voigt profiles were used; the cell parameters, zero shift, peak-width, profile-mixing and asymmetry parameters and a Chebyshev background were refined. The fits are shown in Figures S9 and S10.

3.2. Compound Preparation

3.2.1. Synthesis of p-H_2pbm

N,N′-(1,4-Phenylene)bis(maleamic acid) (*p*-H_2pbm) was prepared as follows.*p*-Phenylenediamine (0.54 g, 5.0 mmol) was dissolved in dichloromethane (DCM, 50 mL) at room temperature in a round-bottom flask and stirred magnetically for 10 min. Once fully dissolved, maleic anhydride (0.980 g, 10.0 mmol) was added in one portion, and the reaction mixture was stirred at room temperature for 2 h. The resulting yellow precipitate was collected by Büchner filtration, washed with distilled water (3 × 30 mL), and dried in an oven at 60 °C for 24 h. Yield 45%. Anal. Calc. for *p*-H_2pbm: C, 55.27; H, 3.98; and N, 9.21. Found: C, 55.07; H, 4.04; and N, 9.08%. Selected IR data (KBr, cm^{-1}): major peaks at 3180 (b), 1693 (s), 1671 (s), 1532 (m), 1268 (s), and 805 (m). ^{1}H NMR (400 MHz, DMSO-d_6, 298 K): δ 13.11 (br s, 2H, COOH), 10.44 (s, 2H, NH), 7.59 (s, 4H, ArH), 6.46 (d, J = 12.1 Hz, 2H, CH=CHCOOH), and 6.31 (d, J = 12.1 Hz, 2H, CH=CHCOOH). ^{13}C NMR (101 MHz, DMSO-d_6, 298 K): δ 166.8 (COOH), 163.0 (CONH), 134.5 (Ar C–N), 131.5 (CH=), 130.7 (=CH), and 120.0 (Ar CH).

3.2.2. Synthesis of $[Zn_2$(p-pbm)$_2(DMF)_2]\cdot DMF\cdot H_2O$ (OnG7-Zn)

Zinc(II) acetate dihydrate ($Zn(OAc)_2\cdot 2H_2O$, 0.220 g, 1.00 mmol) was added to a solution of *p*-H_2pbm (0.206 g, 0.68 mmol) in DMF (5 mL). The mixture was sonicated for 1 min, sealed in a glass vial, and heated at 100 °C for 30 min. After cooling to room temperature, crystals of OnG7-Zn were isolated by filtration, washed with DMF (3 × 2 mL), and dried under vacuum. Yield 25%. Anal. Calc. for $C_{37}H_{43}N_7O_{16}Zn_2$ (OnG7-Zn): C, 45.70;

H, 4.46; and N, 10.08. Found: C, 45.23; H, 4.57; and N, 9.86%. Selected IR data (KBr, cm^{-1}): major peaks at 3350 (b), 1660 (s), 1555 (s), 1385 (s), and 1225 (w).

3.2.3. Synthesis of $[Co_2(p\text{-}pbm)_2(DMF)_2]\cdot DMF\cdot H_2O$ (OnG7-Co)

The synthesis of OnG7-Co followed the same general procedure as for OnG7-Zn, with minor modifications. Cobalt(II) acetate dihydrate ($Co(OAc)_2\cdot 2H_2O$, 0.180 g, 0.85 mmol) was added to a solution of *p*-H_2pbm (0.206 g, 0.68 mmol) in *N*,*N*-dimethylformamide (DMF, 20 mL). The mixture was sonicated for 1 min, sealed in a glass vial, and heated at 100 °C for 3 h. Upon cooling to room temperature, green plate-like crystals of OnG7-Co were isolated by filtration, washed with DMF (3 × 5 mL), and dried under vacuum. Yield 20%. Anal. Calc. for OnG7-Co: C, 46.31; H, 4.52; and N, 10.22. Found: C, 46.59; H, 4.99; and N, 10.02%. Selected IR data (KBr, cm^{-1}): major peaks at 3360 (b), 1650 (s), 1550 (s), 1380 (s), and 1210 (w).

3.2.4. Synthesis of $[Cu_2(p\text{-}pbm)_2(DMF)_2]\cdot DMF\cdot H_2O$ (OnG7-Cu)

Copper(II) acetate monohydrate ($Cu(OAc)_2\cdot H_2O$, 0.440 g, 2.20 mmol) was added to a solution of *p*-H_2pbm (0.206 g, 0.68 mmol) in *N*,*N*-dimethylformamide (DMF, 20 mL). The mixture was sonicated for 1 min, sealed in a glass vial, and heated at 100 °C for 24 h. After cooling to room temperature, a crystalline green powder of OnG7-Cu was isolated by filtration, washed with DMF (3 × 5 mL), and dried under vacuum. Yield 25%. Anal. Calc. for OnG7-Cu: C, 45.87; H, 4.47; and N, 10.12. Found: C, 46.03; H, 4.25; and N, 10.28%. Selected IR data (KBr, cm^{-1}): major peaks at 3360 (b), 1650 (s), 1550 (s), 1380 (s), and 1210 (w).

3.3. Single-Crystal X-Ray Crystallography

Single-crystal diffraction data for OnG7-Zn were collected on a Rigaku diffractometer equipped with a HyPix detector and a Cu Kα radiation source (λ = 1.54184 Å). The selected crystal was an orange block (0.04 × 0.01 × 0.01 mm^3) and was maintained at 150.0(2) K during data collection. Data collection, cell refinement and data reduction were performed using CrysAlisPro 1.171.42.79a, with a multi-scan absorption correction. The structure was solved by direct methods using SHELXS [44] and refined by full-matrix least squares on F^2 using SHELXL 2018/3 [45] within Olex2 1.5 [46].

All non-hydrogen atoms were refined anisotropically. Carbon-bound H atoms included in the model were placed in geometrically calculated positions and refined using a riding model, whereas the lattice-water H atoms were refined with restraints. The four amide H atoms and the formyl H atoms of the two coordinated DMF ligands were not included in the deposited model. The chemical formulation $[Zn_2(p\text{-}pbm)_2(DMF)_2]\cdot DMF\cdot H_2O$ corresponds to $C_{37}H_{43}N_7O_{16}Zn_2$; and the six omitted H atoms account for the lower H count in the deposited atom model, $C_{37}H_{37}N_7O_{16}Zn_2$. The complete chemical formula is used for the elemental-analysis calculations.

Due to the small size and poor diffraction quality of the OnG7-Co and OnG7-Cu crystals, attempts to obtain single-crystal structures were unsuccessful despite multiple crystallisation trials. The polycrystalline samples were instead examined by powder X-ray diffraction (PXRD). As shown in Figure S1, the experimental PXRD patterns of OnG7-Co and OnG7-Cu display diffraction features similar to those of OnG7-Zn, supporting structural similarity across the series.

The experimental OnG7-Zn PXRD pattern agrees with the pattern calculated from its single-crystal structure in the positions of several prominent reflections (Figure S6). Experimental maxima near 8.01°, 9.40° and 11.27° 2θ correspond to calculated Cu $K\alpha_1$ positions near 8.11°, 9.43° and 11.28°, respectively. The as-synthesised pattern is well described by

Le Bail fitting over 5.1–40° 2θ using a triclinic cell refined from the single-crystal starting parameters (Rwp = 6.8%; Figure S9), which is consistent with a single crystalline phase. The PXRD data were collected at room temperature, whereas the single-crystal structure was determined at 150.0(2) K. The room-temperature cell obtained from the Le Bail fit ($V = 1265.2$ Å^3) is expanded relative to the 150 K single-crystal cell ($V = 1207.8$ Å^3) by 4.8%, mainly along a (+2.2%) and b (+1.5%), with c almost unchanged (+0.3%). This anisotropic expansion accounts for the shifts in peak position. It is consistent with thermal expansion between 150 K and room temperature, and differences in guest content between the single crystal and the bulk powder may also contribute. The reflection-dependent differences in relative intensity are consistent with a possible preferred-orientation contribution from non-random alignment of crystallites in the unground specimen. An exploratory structure-constrained comparison improved when a preferred-orientation correction was included. The crystal faces were not indexed, so a specific preferred face cannot be assigned. Differences in guest content may also contribute.

Table S1 lists the unit-cell parameters and refinement details for OnG7-Zn. The CIF is available free of charge from the Cambridge Crystallographic Data Centre (CCDC), UK (https://www.ccdc.cam.ac.uk/structures/ (accessed on 8 November 2026)), under deposition number 2520844.

3.4. Drug Uptake and Release Studies

OnG7-Zn (20 mg) was suspended in DMF (10 mL) in a 20 mL glass vial and stirred at 500 rpm at room temperature for 24 h. The suspension was centrifuged (4000 rpm, 5 min) and the supernatant removed. The solid was resuspended in acetone (10 mL), stirred at 500 rpm at room temperature for a further 24 h, centrifuged again (4000 rpm, 5 min) and dried at 70 °C for 24 h in an open vial in a convection oven.

The 6-Mercaptopurine monohydrate (6MP·H_2O, 30 mg) was introduced into ethanol (10 mL; nominal added concentration 3.0 mg mL^{-1}) and stirred at room temperature. The solvent-exchanged and dried OnG7-Zn (10 mg) was added and the mixture was stirred continuously at room temperature for 7 days. At defined time intervals, aliquots were withdrawn and centrifuged, and the supernatants were analysed by UV–vis spectroscopy at 310 nm. For release experiments, the resulting 6MP@OnG7-Zn material was filtered, thoroughly washed with ethanol and dried under vacuum. The designation 6MP@OnG7-Zn refers here to this recovered, washed material. Release was performed in phosphate-buffered saline (PBS, pH 7.4) at 37 °C and monitored by UV–vis spectroscopy.

4. Conclusions

The symmetric linker p-H_2pbm, N,N′-(1,4-phenylene)bis(maleamic acid), has been used to prepare the OnG7-M coordination-framework family (M = Zn, Co, and Cu). Single-crystal X-ray diffraction of OnG7-Zn establishes a four-connected sql layer built from $[Zn_2(COO)_4(DMF)_2]$ paddlewheel nodes linked by ditopic p-pbm^{2-} ligands. Short interlayer amide-N···O contacts are consistent with hydrogen bonding, although the amide H positions were not determined. PXRD supports structural similarity of the Co(II) and Cu(II) analogues; their structures have not been independently determined by single-crystal diffraction. OnG7 is the first family of MOFs bearing p-H_2pbm in its neutral or ionic form.

Selected properties were examined in two members of this family. The PXRD pattern of as-synthesised OnG7-Zn is consistent with a single crystalline phase, while activation retains a parent-related crystalline component accompanied by a partial structural change. Initial uptake/release experiments with solvent-exchanged and dried OnG7-Zn showed a 53.4% decrease in supernatant absorbance over 7 days and rapid release of 6-mercaptopurine from the recovered material in phosphate-buffered saline at 37 °C. OnG7-Cu showed antifer-

romagnetic coupling, J = −158 cm^{-1}, consistent with exchange within a carboxylate-bridged Cu(II) dimer. The thermogravimetric profiles contain multiple mass-loss steps, with solvent removal and possible decomposition contributions that cannot be resolved independently from TGA alone.

This study extends the coordination chemistry of a symmetric bis(maleamate) linker to a related two-dimensional framework family, combining structural analysis with initial characterisation of metal-dependent properties. Future work can examine guest interactions and stability under matched conditions to establish the scope of this linker environment for uptake and release applications.

Supplementary Materials: The following supporting information can be downloaded at https://www.mdpi.com/article/10.3390/inorganics14110290/s1. Figure S1: PXRD patterns of OnG7-Zn, OnG7-Co and OnG7-Cu; Figure S2: ^{1}H and $^{13}C\{^{1}H\}$ NMR spectra of p-H_2pbm in DMSO-d_6 at 298 K; Figure S3: FT-IR spectra of OnG7-Zn, OnG7-Co and OnG7-Cu; Figure S4: UV–vis spectra of the ethanolic supernatant during seven days of contact with OnG7-Zn; Figure S5: UV–vis spectra of 6MP released from 6MP@OnG7-Zn in PBS (pH 7.4) at 37 °C; Figure S6: Experimental and calculated PXRD patterns of parent OnG7-Zn; Figure S7: FT-IR spectra of parent OnG7-Zn, recovered and washed 6MP@OnG7-Zn, and free 6MP; Figure S8: PXRD patterns of as-synthesised and activated OnG7-Zn; Figure S9: Le Bail fit of the PXRD pattern of as-synthesised OnG7-Zn; Figure S10: Low-angle region of the Le Bail fit of the activated OnG7-Zn PXRD pattern; Table S1: Crystallographic data and structure refinement parameters for OnG7-Zn; Table S2: Calculated solvent fractions and observed mass losses for the OnG7 series.

Author Contributions: Investigation, D.M., A.K., B.K., J.T. and J.M.; formal analysis, A.K., B.K., J.T. and J.M.; writing—original draft preparation, C.P.; writing—review and editing, D.M., A.K., B.K., J.T., J.M., S.M. and C.P.; supervision, S.M. and C.P.; and project administration, C.P. All authors have read and agreed to the published version of the manuscript.

Funding: This research was funded by Research Ireland, grant numbers 12/RC/2275_P2, GOIPG/2024/2355, and 21/PATH-S/9454.

Institutional Review Board Statement: Not applicable.

Informed Consent Statement: Not applicable.

Data Availability Statement: The original contributions presented in this study are included in the article/supplementary material. Further inquiries can be directed to the corresponding author. The crystallographic data for OnG7-Zn have been deposited with the Cambridge Crystallographic Data Centre under deposition number CCDC 2520844.

Conflicts of Interest: The authors declare no conflicts of interest.

References

1. Yusuf, V.F.; Malek, N.I.; Kailasa, S.K. Review on Metal–Organic Framework Classification, Synthetic Approaches, and Influencing Factors: Applications in Energy, Drug Delivery, and Wastewater Treatment. *ACS Omega* **2022**, *7*, 44507–44531. [CrossRef] [PubMed]
2. Yuan, S.; Feng, L.; Wang, K.; Pang, J.; Bosch, M.; Lollar, C.; Sun, Y.; Qin, J.; Yang, X.; Zhang, P.; et al. Stable Metal–Organic Frameworks: Design, Synthesis, and Applications. *Adv. Mater.* **2018**, *30*, 1704303. [CrossRef] [PubMed]
3. Eddaoudi, M.; Moler, D.B.; Li, H.; Chen, B.; Reineke, T.M.; O'Keeffe, M.; Yaghi, O.M. Modular Chemistry: Secondary Building Units as a Basis for the Design of Highly Porous and Robust Metal−Organic Carboxylate Frameworks. *Acc. Chem. Res.* **2001**, *34*, 319–330. [CrossRef] [PubMed]
4. Zhou, H.-C.J.; Kitagawa, S. Metal–Organic Frameworks (MOFs). *Chem. Soc. Rev.* **2014**, *43*, 5415–5418. [CrossRef] [PubMed]
5. Furukawa, H.; Cordova, K.E.; O'Keeffe, M.; Yaghi, O.M. The Chemistry and Applications of Metal-Organic Frameworks. *Science* **2013**, *341*, 1230444. [CrossRef] [PubMed]
6. Zhao, M.; Huang, Y.; Peng, Y.; Huang, Z.; Ma, Q.; Zhang, H. Two-dimensional metal–organic framework nanosheets: Synthesis and applications. *Chem. Soc. Rev.* **2018**, *47*, 6267–6295. [CrossRef] [PubMed]

7. Chakraborty, G.; Park, I.-H.; Medishetty, R.; Vittal, J.J. Two-Dimensional Metal-Organic Framework Materials: Synthesis, Structures, Properties and Applications. *Chem. Rev.* **2021**, *121*, 3751–3891. [CrossRef] [PubMed]
8. Wang, P.; Yang, C.; Yao, J.; Li, H.; Hu, Z.; Li, Z. Two-dimensional metal organic framework nanosheets in electrocatalysis. *Chem. Sci.* **2025**, *16*, 6583–6597. [CrossRef] [PubMed]
9. Wang, Y.; Ma, J.; Jin, F.; Li, T.; Javanmardi, N.; He, Y.; Zhu, G.; Zhang, S.; Xu, J.-D.; Wang, T.; et al. Recent Advances in the Synthesis and Application of Monolayer 2D Metal-Organic Framework Nanosheets. *Small Sci.* **2024**, *4*, 2400132. [CrossRef] [PubMed]
10. Ahmed, A.; McHugh, D.; Papatriantafyllopoulou, C. Synthesis and Biomedical Applications of Highly Porous Metal–Organic Frameworks. *Molecules* **2022**, *27*, 6585. [CrossRef] [PubMed]
11. Ahmed, A.; Efthymiou, C.G.; Sanii, R.; Patyk-Kazmierczak, E.; Alsharabasy, A.M.; Winterlich, M.; Kumar, N.; Sensharma, D.; Tong, W.; Guerin, S.; et al. NUIG4: A biocompatible pcu metal–organic framework with an exceptional doxorubicin encapsulation capacity. *J. Mater. Chem. B* **2022**, *10*, 1378–1385. [CrossRef] [PubMed]
12. Horcajada, P.; Gref, R.; Baati, T.; Allan, P.K.; Maurin, G.; Couvreur, P.; Férey, G.; Morris, R.E.; Serre, C. Metal–Organic Frameworks in Biomedicine. *Chem. Rev.* **2012**, *112*, 1232–1268. [CrossRef] [PubMed]
13. Gupta, D.K.; Kumar, S.; Wani, M.Y. MOF magic: Zirconium-based frameworks in theranostic and bio-imaging applications. *J. Mater. Chem. B* **2024**, *12*, 2691–2710. [CrossRef] [PubMed]
14. Li, D.; Yadav, A.; Zhou, H.; Roy, K.; Thanasekaran, P.; Lee, C. Advances and Applications of Metal-Organic Frameworks (MOFs) in Emerging Technologies: A Comprehensive Review. *Glob. Chall.* **2024**, *8*, 2300244. [CrossRef] [PubMed]
15. Vikal, A.; Maurya, R.; Patel, P.; Paliwal, S.R.; Narang, R.K.; Gupta, G.D.; Kurmi, B.D. Exploring metal-organic frameworks (MOFs) in drug delivery: A concise overview of synthesis approaches, versatile applications, and current challenges. *Appl. Mater. Today* **2024**, *41*, 102443. [CrossRef]
16. Khafaga, D.S.R.; El-Morsy, M.T.; Faried, H.; Diab, A.H.; Shehab, S.; Saleh, A.M.; Ali, G.A.M. Metal–organic frameworks in drug delivery: Engineering versatile platforms for therapeutic applications. *RSC Adv.* **2024**, *14*, 30201–30229. [CrossRef] [PubMed]
17. Wang, H.-S. Metal–organic frameworks for biosensing and bioimaging applications. *Coord. Chem. Rev.* **2017**, *349*, 139–155. [CrossRef]
18. Mohanty, B.; Kumari, S.; Yadav, P.; Kanoo, P.; Chakraborty, A. Metal-organic frameworks (MOFs) and MOF composites based biosensors. *Coord. Chem. Rev.* **2024**, *519*, 216102. [CrossRef]
19. Elgazar, A.; Sabouni, R.; Ghommem, M.; Majdalawieh, A.F. Novel metal–organic framework biosensing platform for detection of COVID-19 RNA. *Sci. Rep.* **2024**, *14*, 25437. [CrossRef] [PubMed]
20. Nguyen, N.T.T.; Nguyen, T.T.T.; Ge, S.; Liew, R.K.; Nguyen, D.T.C.; Tran, T.V. Recent progress and challenges of MOF-based nanocomposites in bioimaging, biosensing and biocarriers for drug delivery. *Nanoscale Adv.* **2024**, *6*, 1800–1821. [CrossRef] [PubMed]
21. Chattopadhyay, K.; Mandal, M.; Maiti, D.K. A review on zirconium-based metal–organic frameworks: Synthetic approaches and biomedical applications. *Mater. Adv.* **2024**, *5*, 51–67. [CrossRef]
22. Quijia, C.R.; Lima, C.; Silva, C.; Alves, R.C.; Frem, R.; Chorilli, M. Application of MIL-100(Fe) in drug delivery and biomedicine. *J. Drug Deliv. Sci. Technol.* **2021**, *61*, 102217. [CrossRef]
23. Wang, Y.; Tang, Y.; Guo, L.; Yang, X.; Wu, S.; Yue, Y.; Xu, C. Recent advances in zeolitic imidazolate frameworks as drug delivery systems for cancer therapy. *Asian J. Pharm. Sci.* **2025**, *20*, 101017. [CrossRef] [PubMed]
24. Markopoulou, P.; Panagiotou, N.; Li, A.; Bueno-Perez, R.; Madden, D.; Buchanan, S.; Fairen-Jimenez, D.; Shiels, P.G.; Forgan, R.S. Identifying Differing Intracellular Cargo Release Mechanisms by Monitoring In Vitro Drug Delivery from MOFs in Real Time. *Cell Rep. Phys. Sci.* **2020**, *1*, 100254. [CrossRef] [PubMed]
25. Luan, X.; Jin, X.; Li, X.; Dong, J.; Du, X. Physiologically Stable, Epitope-Imprinted, and Double-Gated Metal–Organic Framework Drug Delivery System for Tumor-Targeted Combination Therapy. *ACS Appl. Mater. Interfaces* **2025**, *17*, 34819–34832. [CrossRef] [PubMed]
26. Zeng, R.; He, T.; Lu, L.; Li, K.; Luo, Z.; Cai, K. Ultra-thin metal–organic framework nanosheets for chemo-photodynamic synergistic therapy. *J. Mater. Chem. B* **2021**, *9*, 4143–4153. [CrossRef] [PubMed]
27. Davis, R.; Urbanowski, R.A.; Gaharwar, A.K. 2D layered nanomaterials for therapeutics delivery. *Curr. Opin. Biomed. Eng.* **2021**, *20*, 100319. [CrossRef] [PubMed]
28. Zhong, L.; Yang, T.; Li, P.; Shi, L.; Lai, J.; Gu, L. Metal-Organic Framework-Based Nanotherapeutics with Tumor Hypoxia-Relieving Ability for Synergistic Sonodynamic/Chemo-therapy. *Front. Mater.* **2022**, *9*, 841503. [CrossRef]
29. Sun, Y.; Zheng, L.; Yang, Y.; Qian, X.; Fu, T.; Li, X.; Yang, Z.; Yan, H.; Cui, C.; Tan, W. Metal–Organic Framework Nanocarriers for Drug Delivery in Biomedical Applications. *Nano-Micro Lett.* **2020**, *12*, 103. [CrossRef] [PubMed]
30. Lawson, H.D.; Walton, S.P.; Chan, C. Metal–Organic Frameworks for Drug Delivery: A Design Perspective. *ACS Appl. Mater. Interfaces* **2021**, *13*, 7004–7020. [CrossRef] [PubMed]
31. Forgan, R.S.; Marshall, R.J.; Struckmann, M.; Bleine, A.B.; Long, D.-L.; Bernini, M.C.; Fairen-Jimenez, D. Structure-directing factors when introducing hydrogen bond functionality to metal–organic frameworks. *CrystEngComm* **2015**, *17*, 299–306. [CrossRef]

32. Hashad, N.M.; Nassar, M.Y.; Jahin, H.S.; El-Nahas, A.M.; Adam, M.S.S.; Kamoun, E.A.; Alfurayj, I.; Ayoup, M.S.; El-Demerdash, S.H.; Abou-Elyazed, A.S. Urea-functionalized HKUST-1 metal–organic framework for high-performance lead adsorption. *RSC Adv.* **2025**, *15*, 46523–46540. [CrossRef] [PubMed]
33. Mohamed, A.A.; Al-Halim, I.Z. Comparative Differential Thermal Analysis of Epoxy Resin Blends with Amic Acid-Copper Complexes. *Tikrit J. Pure Sci.* **2008**, *13*, 143–146.
34. Arif, M.; Fatima, U.; Rauf, A.; Farooqi, Z.H.; Javed, M.; Faizan, M.; Zaman, S. A New 2D Metal-Organic Framework for Photocatalytic Degradation of Organic Dyes in Water. *Catalysts* **2023**, *13*, 231. [CrossRef]
35. Kaur, H.; Mohanta, G.C.; Gupta, V.; Kukkar, D.; Tyagi, S. Synthesis and Characterization of ZIF-8 Nanoparticles for Controlled Release of 6-Mercaptopurine Drug. *J. Drug Deliv. Sci. Technol.* **2017**, *41*, 106–112. [CrossRef]
36. Gong, M.; Yang, J.; Li, Y.; Gu, J. Glutathione-Responsive Nanoscale MOFs for Effective Intracellular Delivery of the Anticancer Drug 6-Mercaptopurine. *Chem. Commun.* **2020**, *56*, 6448–6451. [CrossRef] [PubMed]
37. Winterlich, M.; Efthymiou, C.G.; Papawassiliou, W.; Carvalho, J.P.; Pell, A.J.; Mayans, J.; Escuer, A.; Carty, M.P.; McArdle, P.; Tylianakis, E.; et al. A Biocompatible $ZnNa_2$-Based Metal–Organic Framework with High Ibuprofen, Nitric Oxide and Metal Uptake Capacity. *Mater. Adv.* **2020**, *1*, 2248–2260. [CrossRef]
38. Ahmed, A.; Bezrukov, A.; Sensharma, D.; O'Malley, C.; Zaworotko, M.J.; Tiana, D.; Papatriantafyllopoulou, C. Synthesis and Characterisation of Multivariate Metal–Organic Frameworks for Controlled Doxorubicin Absorption and Release. *Molecules* **2025**, *30*, 1968. [CrossRef] [PubMed]
39. Alrashidi, M.; McHugh, K.; Jordan, L.; McHugh, D.; Li, S.; Efthymiou, C.G.; Leonard, D.; Tong, W.; Farras, P.; Dwyer, R.; et al. Expanding the Therapeutic Potential of NUIG4: A Multifunctional Metal–Organic Framework for Dual Anticancer and Antibacterial Drug Delivery. *ChemBioChem* **2026**, *27*, e202500484. [CrossRef] [PubMed]
40. Pui, C.-H.; Evans, W.E. Treatment of Acute Lymphoblastic Leukemia. *N. Engl. J. Med.* **2006**, *354*, 166–178. [CrossRef] [PubMed]
41. Schmiegelow, K.; Nielsen, S.N.; Frandsen, T.L.; Nersting, J. Mercaptopurine/Methotrexate Maintenance Therapy of Childhood Acute Lymphoblastic Leukemia: Clinical Facts and Fiction. *J. Pediatr. Hematol. Oncol.* **2014**, *36*, 503–517. [CrossRef] [PubMed]
42. Chilton, N.F.; Anderson, R.P.; Turner, L.D.; Soncini, A.; Murray, K.S. PHI: A Powerful New Program for the Analysis of Anisotropic Monomeric and Exchange-Coupled Polynuclear d- and f-Block Complexes. *J. Comput. Chem.* **2013**, *34*, 1164–1175. [CrossRef] [PubMed]
43. Bain, G.A.; Berry, J.F. Diamagnetic Corrections and Pascal's Constants. *J. Chem. Educ.* **2008**, *85*, 532. [CrossRef]
44. Sheldrick, G.M. A short history of SHELX. *Acta Crystallogr. A* **2008**, *64*, 112–122. [CrossRef] [PubMed]
45. Sheldrick, G.M. Crystal structure refinement with SHELXL. *Acta Crystallogr. C Struct. Chem.* **2015**, *71*, 3–8. [CrossRef] [PubMed]
46. Dolomanov, O.V.; Bourhis, L.J.; Gildea, R.J.; Howard, J.A.K.; Puschmann, H. OLEX2: A Complete Structure Solution, Refinement and Analysis Program. *J. Appl. Cryst.* **2009**, *42*, 339–341. [CrossRef]

Disclaimer/Publisher's Note: The statements, opinions and data contained in all publications are solely those of the individual author(s) and contributor(s) and not of MDPI and/or the editor(s). MDPI and/or the editor(s) disclaim responsibility for any injury to people or property resulting from any ideas, methods, instructions or products referred to in the content.